JVST A
Journal of Vacuum Science & Technology A

Area-selective aerosol jet fog deposition: Advancing large-area and sustainable fabrication

Cite as: J. Vac. Sci. Technol. A **39**, 013407 (2021); https://doi.org/10.1116/6.0000642
Submitted: 17 September 2020 . Accepted: 30 November 2020 . Published Online: 23 December 2020

Kamesh Mullapudi, Nishit M. Murari, Ryan H. Mansergh, Douglas A. Keszler, and John F. Conley

JVST A
Journal of Vacuum Science & Technology A

ARTICLE

avs.scitation.org/journal/jva

Area-selective aerosol jet fog deposition: Advancing large-area and sustainable fabrication

Cite as: J. Vac. Sci. Technol. A 39, 013407 (2021); doi: 10.1116/6.0000642
Submitted: 17 September 2020 · Accepted: 30 November 2020 ·
Published Online: 23 December 2020

Kamesh Mullapudi,[1] Nishit M. Murari,[1] Ryan H. Mansergh,[2] Douglas A. Keszler,[2] and John F. Conley, Jr.[1,a)]

AFFILIATIONS

[1]School of Electrical Engineering and Computer Science, Oregon State University, Corvallis, Oregon 97331
[2]Department of Chemistry, Oregon State University, Corvallis, Oregon 97331

Note: This paper is a part of the Special Topic Collection on Area Selective Deposition.
[a)]**Author to whom correspondence should be addressed:** jconley@eecs.oregonstate.edu

ABSTRACT

In this work, we demonstrate controlled area-selective deposition of aluminum oxide phosphate (AlPO) at room temperature and near atmospheric pressure using a potentially zero-waste aerosol jet fog (ajFOG) deposition system. Octyl-trichlorosilane (OTS-8) self-assembled monolayers (SAMs) are coated on SiO_2/Si substrates to form a blanket hydrophobic functionalization. Next, ultraviolet/ozone exposure through a shadow mask removes OTS-8 in the exposed regions, creating a pattern of hydrophobic and hydrophilic regions. AlPO is selectively deposited onto the hydrophilic regions from an aqueous aerosol precursor fog of aluminum phosphate inorganic clusters. Smooth films with sharp boundaries are deposited. The AlPO features and defects in the hydrophobic areas are investigated as a function of feature size, SAM type/application method/exposure time, ajFOG process parameters, and underlying substrate.

I. INTRODUCTION

Area-selective deposition (ASD), the direct deposition of materials only on desired areas of a substrate, has recently emerged as a way to overcome some of the drawbacks of conventional top-down lithography. Instead of top-down masks, surface selectivity is exploited to directly pattern a film as it is deposited. Lower costs may be achieved by reducing the number of conventional lithographic sequences as well as material wasted per mask step.[1] Although the focus of recent efforts have been on nanoscale patterning for microelectronics,[2] ASD is also appealing for large-area electronics such as displays,[3] patterning for flip-chip packaging of ICs,[4] and microelectromechanical systems (MEMS) where feature sizes are of the order of tens of micrometers. Methods of inducing surface selectivity include plasma treatments,[5–7] chemoselective inhibitors,[8] chemically amplified photoresists,[9] inherently selective deposition chemistry,[10] polymer brushes,[11] and self-assembled monolayers (SAMs). SAMs are formed by molecules made up of three parts: a head group, an alkane chain backbone, and a tail group. Van der Waals interactions between the chains promote the formation of an ordered monolayer of these molecules. Typically, the head group attaches to a hydrophilic surface on the substrate with the tail group facing outward to create a new hydrophobic surface. Hydrophobic SAMs have been demonstrated to inhibit nucleation during atomic layer deposition (ALD), and recently many groups have reported area-selective (AS) ALD processes using patterned SAMs.[12–17] While this work has shown great promise, the microelectronics, photovoltaics, and display industries are seeking alternatives to vacuum-based deposition techniques as well as flexible substrate compatible temperatures. Solution-based deposition techniques may lower costs, reduce temperatures, and enable more environmentally sustainable approaches. However, solution deposition, primarily represented by conventional spin-coating, is typically limited to planar substrates and lacks the ability to form uniform films over large surface areas. A new aerosol-based technique, aerosol jet fog (ajFOG) deposition, overcomes the limitations of spin-coating as well as other mist-based deposition techniques by employing a novel atomizer consisting of two opposing jets located within the deposition chamber. This atomizer configuration generates a uniform mist/fog that is scalable to arbitrarily large substrate areas and has enabled excellent control over film thickness ranging from ~1 μm down to a few nanometers.[18,19] In addition, the head-on collision of the precursor streams shears droplets into a fine fog, allowing the use of low volatility aqueous-

based precursors that have been demonstrated to produce Al_2O_3 films with properties comparable to ALD.[20]

Aluminum oxide phosphate (AlPO) is a wide bandgap (~7.6 eV) insulator with a process dependent electron affinity ranging from 0.72 to 1.42 eV.[21,22] AlPO has shown promise as a gate insulator for thin film transistors,[23,24] a cathode coating in lithium-ion batteries,[25,26] an inorganic resist,[27] blocking and tunneling layers in memory devices,[28] and a catalyst for the conversion of methanol to dimethyl ether.[29]

In this work, area-selective ajFOG (AS-ajFOG) deposition of AlPO is demonstrated at room temperature and near atmospheric pressure using a recyclable/reusable aqueous precursor. Octyl-trichlorosilane (OTS-8)-based SAMs are combined with shadow masked ultraviolet (UV)/ozone (O_3) exposure to create hydrophobic and hydrophilic regions on an SiO_2/Si wafer. Selectively deposited AlPO features on hydrophilic areas and AlPO defects on hydrophobic areas are investigated as a function of feature size, choice of SAM type (OTS-8 versus OTS-18), SAM application method, SAM exposure time, ajFOG process parameters, and underlying substrate.

II. EXPERIMENTAL DETAILS

An aqueous AlPO precursor [$Al_5O_3(PO_4)_3$] was synthesized using aluminum nitrate (98% Sigma Aldrich), nitric acid (99.9% Alfa Aesar), and de-ionized (DI) water (18.2 MΩ).[23] The final precursor solution was diluted to 0.4M and filtered with a 0.2-μm polytetrafluoroethylene filter.

Deposition of AlPO thin films was conducted using a Beneq ACS 200-101 ajFOG deposition system.[18,19] Figure 1 shows a simplified schematic illustrating operation of the ACS 200-101. As shown in Fig. 1(a), the system generates an aerosol fog at room temperature and slightly below atmospheric pressure via an *in situ* atomizer composed of two impinging jets. Separate dosing diaphragm pumps supply each nozzle with fresh precursor solution to produce high-velocity jets of fine precursor droplets. These droplets collide head-on, undergoing a secondary atomization to shear into even finer aqueous droplets to produce a flat and evenly distributed aerosol disk inside the chamber. Over time, momentum carries these droplets throughout the chamber to create a homogeneous precursor fog. Thin film deposition on a substrate may be performed in either the "continuous" mode or the "pulse" mode. In continuous mode, the substrate is introduced into the chamber while the aerosol fog is continuously generated.[19]

In the pulse mode (used exclusively in this work), the aerosol generation is stopped prior to transferring the substrate into the chamber [Fig. 1(b)]. Once the aerosol generation is stopped, the fog density decreases over time as gravity causes droplets to settle gradually to the bottom of the chamber with a characteristic settling time, τ.[18] Due to the interaction between gravity and dispersive thermal motion, larger droplets settle out more quickly on average than smaller droplets. To improve film uniformity, the fog droplets are allowed to stabilize for a specified wait time, t_w, before introducing the wafer into the chamber as shown in Fig. 1(b). In this work, the fog was found to be completely dissipated after about 600 s. t_w thus influences the thickness of the film deposited.[18]

The substrate is introduced into the chamber via a load lock, which is kept at a slightly positive pressure with respect to the chamber to prevent the aerosol fog from leaking into the load lock. After a specified exposure time, t_{exp}, the coated substrate is transferred from the chamber back into the load lock. When removed from the chamber, the film is wet and susceptible to air turbulence. To prevent rapid film drying and to promote spreading and uniformity, the load lock is supplied with moist N_2 (g). The coated substrate rests in the load lock for a set "leveling" time (typically 30 s), allowing the droplets to coalesce, dry, and form a continuous film.[18] Following leveling, the coated substrate is removed from the load lock and cured on a hotplate at 300 °C for 1 min. A complete deposition, which includes fog formation, mist settling/wait time, leveling, and exposure, takes ~10 min. We have shown previously that the thickness, d_{ox}, of blanket deposited ajFOG AlPO films

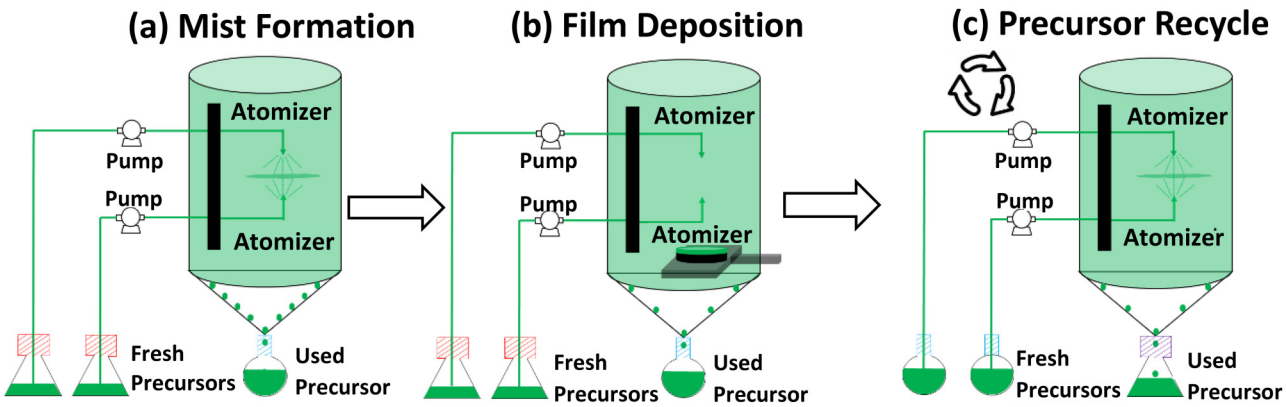

FIG. 1. Schematic illustration of the ajFOG thin film deposition process used in this work. (a) Aerosol mist formation from fresh precursor (excess precursor is collected at the bottom of the chamber). (b) Film deposition in pulse mode: Aerosol generation is stopped after 2 min. After a settling time, t_w, a wafer is introduced into the chamber for an exposure time, t_{exp}, during which film is coated with falling mist. (c) Collected excess precursor may be recycled and reused.

depends on precursor concentration ([N]), t_w, and t_{exp}, and may be estimated by

$$d_{blanket} = C_{sat} \cdot [\mathrm{N}] \cdot e^{-t_w/\tau} \cdot (1 - e^{-t_{exp}/\tau}), \quad (1)$$

where $C_{sat} = 420$ nm/M (for $t_w = 0$ and $t_{exp} = \infty$), and $\tau = 100$ s.[18] In this work, unless otherwise specified, [N] = 0.4M, $t_w = 120$ s, and t_{exp} was adjusted to achieve the desired thickness.

During an ajFOG deposition run, the precursor fog coats not only the wafer but also the inside of the chamber. The precursor that does not end up on the wafer flows down the walls of the chamber and out through a drain at the bottom where it is collected in a clean reservoir, shown as round-bottom flasks in Fig. 1(c). This precursor may then be recycled. As discussed in the supplementary material (Fig. S1),[30] the collected precursor shows no apparent deterioration as compared to unused precursor and films deposited from unused and recycled precursor show similar composition, thickness, and uniformity.

For uniform ajFOG film deposition, a uniformly hydrophilic starting surface is critical. Prior to all depositions, silicon (100) wafers were cleaned by ultra-sonicating in acetone, isopropanol, and de-ionized water for 5 min each, followed by 15 min of oxygen plasma treatment in a Plasma Etch Inc. PE 50. This treatment was found to produce a uniformly hydrophilic surface, as assessed by DI water contact angle measurements in which a contact angle could not be measured due to droplet wetting of the surface.

For area-selective deposition, the hydrophilic surface was patterned with hydrophobic regions using a 1 mM solution of OTS-8 in chloroform. OTS-8 consists of a trichlorosilane head group and a hydrophobic CH_3 tail group. An OTS-8 SAM was first uniformly applied to a cleaned wafer surface either by (i) spin-coating at 3000 rpm for 10 s followed by a toluene wash and drying on a hotplate for 10 min at 100 °C or (ii) immersion in OTS-8 solution for 8–72 h. Unless otherwise indicated, spin-coating was used. OTS-8 was then selectively removed from the surface by 10 min exposure to UV/O_3 (using a Novascan PSD series benchtop UV-ozone cleaner) through a shadow mask with circular dot openings of radii, r_{mask}, decreasing from 500 to 18.75 μm.

Optical microscope images were acquired using an Axiotron optical microscope. The average areal density, number, shape, and size distribution of defect islands were estimated from their contours using IMAGEJ software processing of optical microscope images, averaging multiple 1.3 mm^2 areas at 5× magnification.[31]

Spectroscopic ellipsometry (J.A. Woollam Co., Inc., M-2000) was used to measure blanket film thickness. The quality and coverage of the SAM coating was assessed with water contact angle measurements using a First Ten Angstroms FTA135. Scanning electron microscopy (SEM) and energy dispersive spectroscopy (EDS) elemental analysis were conducted using FEI QUANTA 3D dual beam SEM/EDS. Profilometric measurements were conducted on a KLA Tencor Alpha Step 500 surface profilometer.

III. RESULTS AND DISCUSSION

A. Selective deposition

Hydrophobic surfaces prevent surface wetting and thin film nucleation of the aqueous AlPO precursor. This sensitivity to surface hydrophilicity/hydrophobicity was exploited to perform AS-ajFOG deposition. The deposition steps are schematically illustrated in Fig. 2: (a) Sequential cleaning of silicon wafer in an ultrasonic bath using acetone, isopropanol, and water, followed by 5 min of oxygen plasma produced a hydrophilic surface. Contact angle measurements could not be measured due to high hydrophilicity. (b) Next, the wafer was either spin coated with or soaked in a 1-mM OTS-8 solution in chloroform, which resulted in a hydrophobic SAM uniformly blanketing the surface of the wafer. A high water contact angle (101°, see the inset), indicated the development of an extremely hydrophobic surface. (c) Following SAM formation, the surface was then exposed to UV/O_3 through a shadow mask in order to (d) selectively remove the SAM from predefined areas and effectively restore the initial hydrophilic surface in the exposed areas. (e) ajFOG deposition was performed on the hydrophilic/hydrophobic patterned wafer followed by a curing step at 300 °C for 1 min, resulting in AlPO thin film formation in the hydrophilic regions. Finally, a successive UV/O_3 exposure for 15 min (not shown) removed the remaining SAM on the selective area deposited substrate.

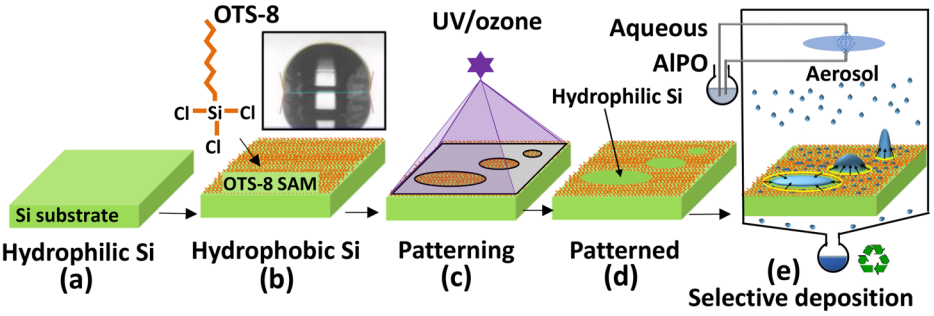

FIG. 2. (Color online) Schematic illustration of the AS-ajFOG thin film deposition process. Illustrated are (a) the initial oxygen plasma cleaned hydrophilic silicon wafer, (b) hydrophobic modification by coating with an OTS-8 SAM (represented by orange molecules on surface), (c) exposure to UV/O_3 through a shadow mask to selectively remove areas of SAM and restore hydrophilicity, (d) patterned hydrophilic/hydrophobic surface, and (e) area-selective AlPO thin film deposition at the hydrophilic sites using the ajFOG system.

When a hydrophilic/hydrophobic patterned substrate is introduced into the chamber, suspended droplets of precursor from the fog settle and coalesce on the hydrophilic regions of the wafer to form defined areas of continuous thin film. In the hydrophobic regions, the fog droplets do not coalesce, remaining as well-formed droplets. Figure 3(a) shows an SEM image of a selectively deposited AlPO thin film "dot" ($t_{exp} = 120$ s) of $r_{dot} \sim 35\,\mu$m and the surrounding "exclusion" region with no AlPO film, in turn surrounded by a region containing small AlPO defect islands. Figure 3(b) shows EDS spectra taken from within a similar dot and just outside the dot in the adjacent exclusion region, at the positions marked in the inset. Within the dot, distinct Al, P, and O peaks from the AlPO film are seen. Just outside the dot, only a weak O peak is detected, attributed to the native SiO_2 layer. The strong Si peak present in both spectra is from the Si substrate. EDS elemental mapping [Fig. 3(c)] shows uniform distribution of Al, P, and O throughout the selectively deposited structure with no segregation. For improved visualization, the elemental image maps superimposed in Fig. 3(c) are individually normalized and plotted in Figs. 3(d)–3(f). The projection of each graph at the top of the z axis matches the image in Fig. 3(c). The sharp boundary of all three elements at the edge of the deposited area indicates the high selectivity of the deposition. The variation in elemental distribution of Al, P, and O along the x and y axes is consistent with tapered edges of the deposited structure, as shown below.

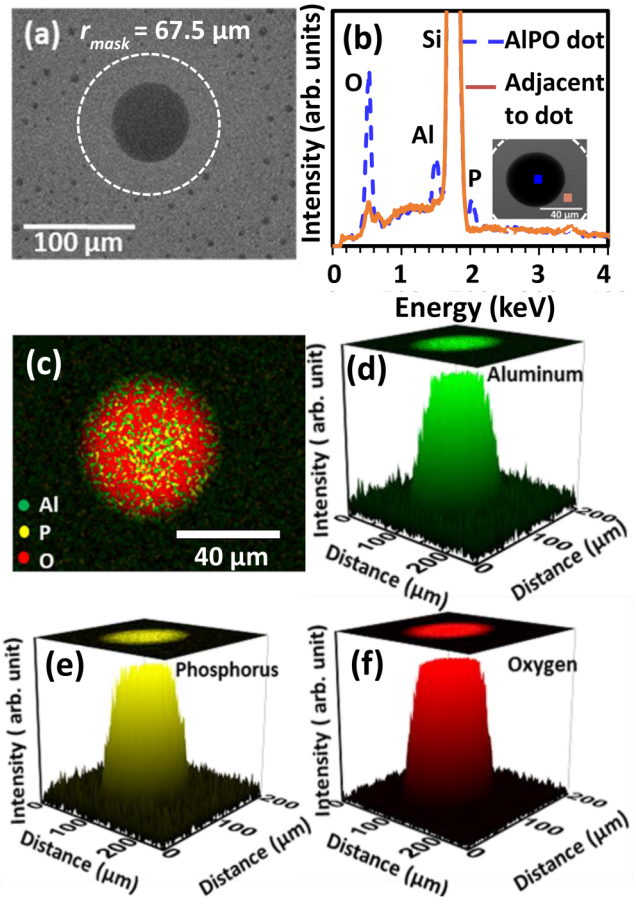

FIG. 3. (Color online) (a) SEM image of a selectively deposited thin film AlPO circular dot. The dashed circle shows the boundary of the defect-free exclusion region. (b) EDS spectra within (blue dashed line) and just outside (orange solid line) of a similar AlPO dot (inset shows the locations used along with the dashed outline of exclusion region). (c) EDS map showing distribution of Al (green), P (yellow), and O (red) within the patterned dot. Individually normalized EDS signal intensity as a function of x and y position for (d) Al, (e) P, and (f) O.

B. Deposited features

Figure 4 shows optical microscope images of a series of AS-ajFOG AlPO dots deposited on the same wafer in the same run

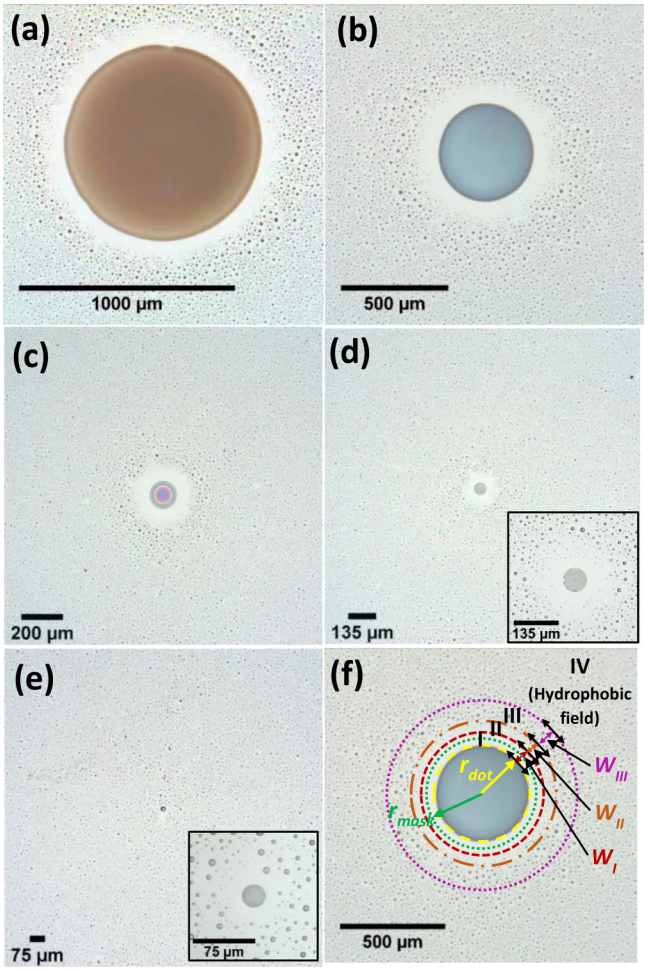

FIG. 4. (Color online) Optical microscope images (5× magnification) of AlPO thin films deposited selectively in circular patterns via ajFOG deposition for r_{mask} openings of (a) 500, (b) 250, (c) 100, (d) 67.5, and (e) 37.5 μm. Insets in (d) and (e) are 20× and 50× magnification images. (f) Illustration of four distinct regions surrounding an $r_{mask} = 250\,\mu$m dot.

using $t_{exp} = 120$ s, covering the range of r_{mask} between 500 and 37.5 μm. While the smallest feature in the shadow mask was $r_{mask} = 18.75\,\mu$m, we observed no deposited features below $r_{mask} = 37.5\,\mu$m. The coloring and distinct "rings" visible in the images in Fig. 4 are concentric interference fringes due to the domed profile of the dots, rather than an actual ringed structure.

Figure 5(a) shows profilometry scans of the dots from Fig. 4, clearly illustrating that the selectively deposited dots have a domed profile with thickness increasing from the border to the center. The small peaks seen at the edges of the profilometry scans are the onset of defects in the hydrophobic region. Figure 5(b) shows that, despite being deposited in the same run, the center height of the deposited AlPO dots, h_{dot}, increases with decreasing r_{dot}, increasing steeply below $r_{mask} = 250\,\mu$m, ranging from $h_{dot} = 67$ nm for $r_{mask} = 500\,\mu$m to as high as $h_{dot} = 1.6\,\mu$m for $r_{mask} = 37.5\,\mu$m. In all cases, h_{dot} is greater than $d_{blanket}$ = 37 nm, the thickness measured for a blanket control film, and also predicted from Eq. (1) for [N] = 0.4M, $t_w = 120$ s, and $t_{exp} = 120$ s. As discussed below, this is due in part to a domed rather than a flat disk-like profile.

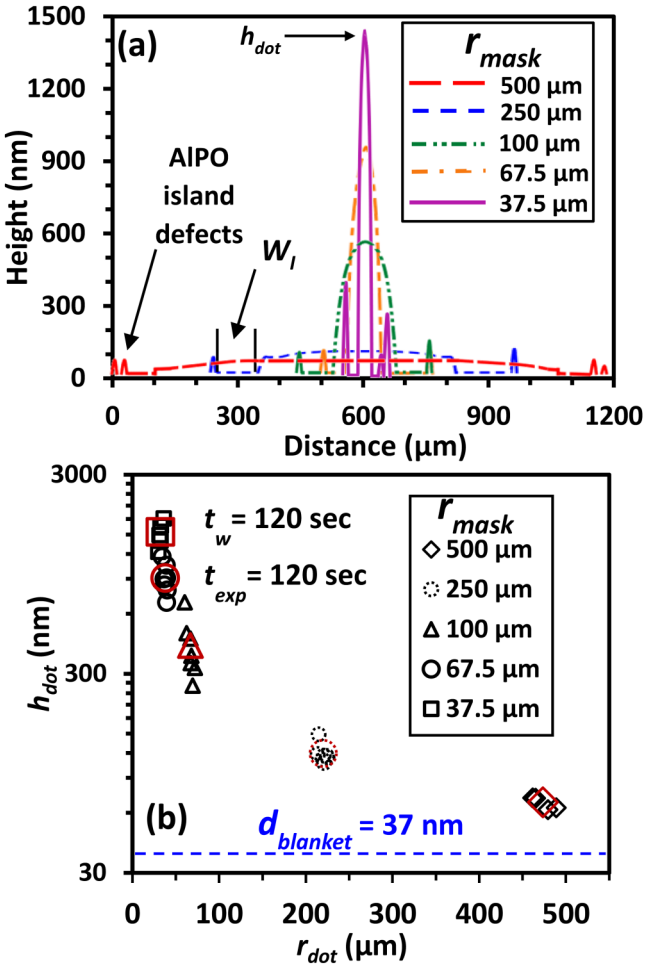

FIG. 5. (Color online) (a) Profilometry scans of deposited dots vs position taken from edges of region II, across region I, and through the center of each dot. The narrow peaks at either end of each plot are due to defects at the border between regions I and II. (b) Plot of h_{dot} vs r_{dot} (blue dashed line indicates expected thickness of blanket film and open red symbols indicate averages).

Figure 4(f) indicates the four distinct regions that surround each patterned dot, independent of r_{dot}: (I) a deposition-free "exclusion region" of width, W_I, that separates the sharp boundary of the selectively deposited AlPO dot from three regions of AlPO defect islands in the surrounding hydrophobic surface, (II) a region of width W_{II} of defects of *smaller* average size, followed by (III) a region of width W_{III} of defects with a *larger* average size, and finally (IV) a "field" region of average size defects spread across the hydrophobic area away from the patterned dots. For the smallest dot, only three regions are apparent: the dot, the exclusion region II, and the field region IV. The exclusion region II and defect regions beyond may also be observed in the SEM image in Fig. 3(a).

The schematic in Fig. 6(a) serves to graphically define various radii and volumes for the following discussion. Shown in Fig. 6(b), W_I was found to increase with increasing r_{dot} (and r_{mask}), from ~15 μm for $r_{mask} = 37.5\,\mu$m saturating at ~50 μm for $r_{mask} = 250$ and 500 μm. For all dots, r_{dot} was significantly smaller than its corresponding r_{mask}. For $t_{exp} = 120$ s, circular r_{mask} openings of 500, (b) 250, (c) 100, (d) 67.5, and (e) 37.5 μm produced r_{dot} of 474, 220, 67, 38, and 19 μm, respectively. The difference $r_{mask} - r_{dot}$ is also plotted versus r_{dot} in Fig. 6(b).

In Fig. 6(c), r_{dot} and $r_{dot} + W_I$ are compared to r_{mask}. The combined total of $r_{dot} + W_I$ is slightly larger than r_{mask}, so that W_I extends into the surrounding hydrophobic region, with $r_{dot} + W_I - r_{mask}$ increasing with r_{mask} [Fig. 6(c)].

It is interesting to compare the actual volume of the deposited dome shaped dots, V_{dot}, to the calculated volumes of disks of the 37 nm blanket film thickness with radii equal to r_{dot}, to r_{mask}, and to $r_{dot} + W_I$, abbreviated as $V_{disk,rdot}$, $V_{disk,rmask}$, and $V_{disk,rdot+WI}$, respectively. As seen in Fig. 6(d), V_{dot} exceeds not only the material available from $V_{disk,rdot}$ and $V_{disk,rmask}$ but also from $V_{disk,rdot+WI}$. The total volume of extra material, $V_{extra} = V_{dot} - V_{disk,rdot}$ is plotted in Fig. 6(d) with the ratio $V_{dot}/V_{disk,rdot}$ shown on the secondary axis. $V_{dot}/V_{disk,rdot}$ increases steeply below $r_{dot} = 250\,\mu$m, mirroring the h_{dot} vs r_{dot} plot from Fig. 5(b) and indicating that the increased h_{dot} of the selectively patterned dots with reduced size is due not only to the increasingly domed shape but also to the proportionally greater amount of extra material incorporated into the dot. The effective radius, r_{eff}, required for a disk of the 37 nm thick blanket film, $V_{disk,reff}$, to equal the volume of V_{dot} {i.e., $r_{eff} = \mathrm{sqrt}[V_{dot}/(\pi\, d_{blanket})]$}, is also plotted in Fig. 6(c).

The r_{eff} for each dot is shown as dashed vertical lines in Fig. 7(a), a plot of the percentage areal defect coverage versus distance from the edge of the dot. For each dot, r_{eff} lies within W_{III} and coincides roughly to the distance where the percentage of defect coverage approaches the average coverage in region IV. Thus, V_{extra} is drawn not only from the hydrophilic and hydrophobic parts of the exclusion region I but also the hydrophobic regions II and III surrounding the patterned feature. Shown in Fig. 7(b) is a plot of average defect radius, $r_{defect,avg}$, versus distance from the dot

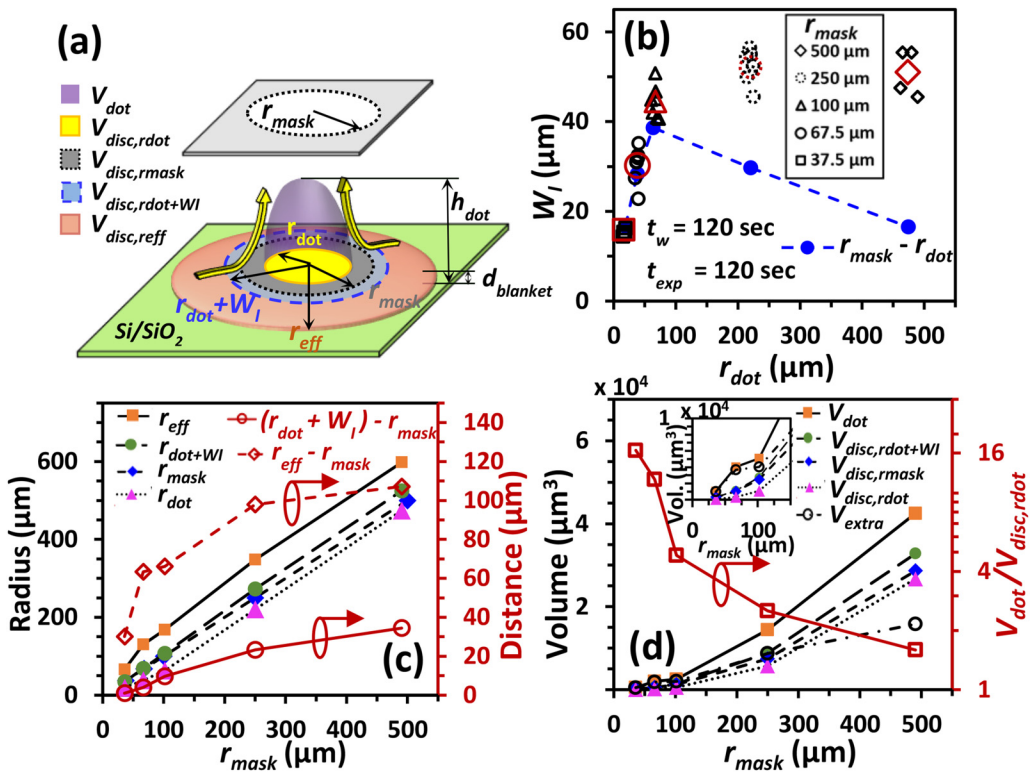

FIG. 6. (Color online) (a) Schematic illustration of V_{dot}, $V_{disk,rdot}$, $V_{disk,rmask}$, $V_{disk,rdot+WI}$, $V_{disk,reff}$, h_{dot}, $d_{blanket}$, r_{mask}, r_{dot}, r_{dot+WI}, and r_{eff}, along with plots of (b) W_I and $r_{mask} - r_{dot}$ vs r_{dot} (large red open symbols indicate averages); (c) r_{dot}, r_{mask}, $r_{dot} + W_I$, r_{eff}, $r_{dot} + W_I - r_{mask}$, r_{eff}, and $r_{eff} - r_{mask}$ vs r_{mask}; (d) V_{dot}, $V_{disk,rdot}$, $V_{disk,rmask}$, $V_{disk,rdot+WI}$, V_{extra}, and ratio $V_{dot}/V_{disk,rdot}$ vs r_{mask}. The inset highlights these parameters for the three smallest dots $r_{mask} = 37.5$, 67.5, and 100 μm.

edge for $r_{mask} = 100\,\mu$m with W_I, W_{II}, and W_{III} indicated as dashed lines and the position of r_{eff} inside region III.

During ajFOG deposition, the precursor droplets falling on the patterned substrate encounter three scenarios: (i) hydrophilic patterned dot areas with a water contact angle near 0°, (ii) hydrophobic field area far away from the patterned hydrophilic dots with a water contact angle of 101°, and (iii) an intermediate region with a surface energy gradient

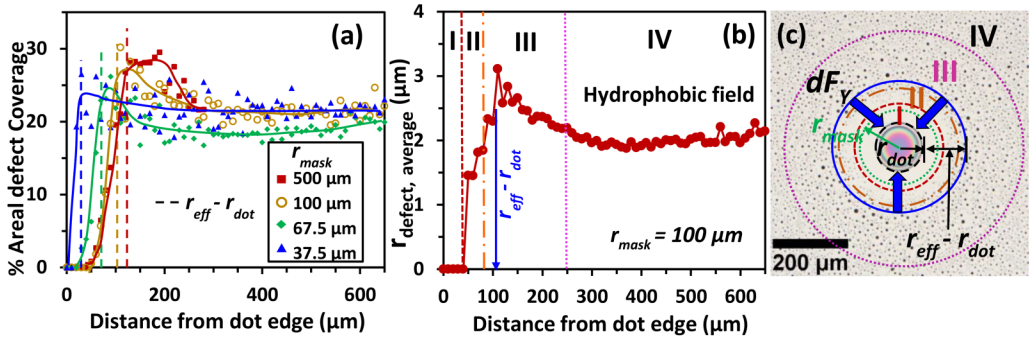

FIG. 7. (Color online) (a) Plot of areal defect coverage (in percent) as a function of distance from the dot edge for various dots ($r_{eff} - r_{dot}$) indicated as color coded dashed lines for each dot (solid lines are to help guide the eye). (b) Plot of mean r_{defect} calculated in 10 μm intervals as a function of distance from dot edge for an $r_{mask} = 100\,\mu$m dot. The four regions are marked and the extracted $r_{eff} - r_{dot}$ is shown by the blue arrow (in region III near the edge of the region II). (c) Illustration of dF_Y originating from a concentric circle of radius r_{eff} (solid blue circle) encompassing regions I (small dashed red circle) and II (dot-dashed orange circle), and a small portion of region III (dotted pink circle) adjacent to region II for the same 100 μm dot; r_{mask} is shown for reference (inner dotted green circle).

that connects the hydrophobic field region to the patterned hydrophilic dots.

The droplets that settle in the hydrophilic patterned dots immediately coalesce to form a bigger droplet. The shape of the coalescing droplet in the hydrophilic region depends on the Laplace length, k^{-1}, of the AlPO precursor,[32]

$$\kappa^{-1} = \sqrt{\frac{\gamma_{LV}}{\rho \cdot g}}, \tag{2}$$

where γ_{LV} and ρ are the surface tension and density of the precursor, respectively, and g is 9.8 m/s^{-2}. For a 0.4 M AlPO solution, it is reasonable to assume γ_{LV} and ρ similar to that of de-ionized water at room temperature and pressure, which yields $\kappa^{-1} \sim 2.7$ mm. Since, all patterned feature sizes, $2r_{mask}$, are below 2.7 mm, the shape of the droplet that forms in the hydrophilic area is solely governed by γ_{LV}, resulting in a spherical cap-like droplet shape of radius $2r_{dot}$ prior to drying and a domed dot shape post-curing.[32]

The droplets that fall on the hydrophobic field region stay relatively stationary and will be discussed further below.

Finally, droplets that fall in the intermediate region experience a surface energy gradient that results in an unbalanced Young's force,

$$dF_Y = \gamma_{LV}(\cos\vartheta_a - \cos\vartheta_r)dx, \tag{3}$$

where θ_a and θ_r are the advancing and receding contact angles in the more and less hydrophilic regions, respectively.[33–35] dF_Y is in the direction toward the more hydrophilic region so that, as illustrated in Fig. 7(c), precursor droplets falling near the edge of the surrounding hydrophobic region move along the surface energy gradient toward the hydrophilic area, where they become incorporated into the patterned dot structure. The domed profile of the dots, the surrounding exclusion region I, and the defect regions II and III are influenced by dF_Y as well as the volume and viscosity of the precursor.

AlPO thin films were also selectively deposited in the shape of lines, squares, and bends as sharp as 90° [Fig. 8(a)]. Linewidths down to 15 μm width could be patterned using a 50 μm wide mask opening. As shown in Fig. 8(b), adjacent features could be patterned as close as ~100 μm apart with clear separation. At about 50 μm and below, adjacent features tended to merge due to the overlapping capillary forces. There appears to be a minimum critical width of the hydrophobic region required to keep adjacent hydrophilic regions separated and distinct during AS-ajFOG deposition. Future work will be required to reduce the minimum line separation (pitch). Improved surface hydrophobicity; precursor parameters such as molarity, solvent, viscosity, and surface tension; and reduced t_{exp} (reduced film thickness) may allow for reduced line separation.

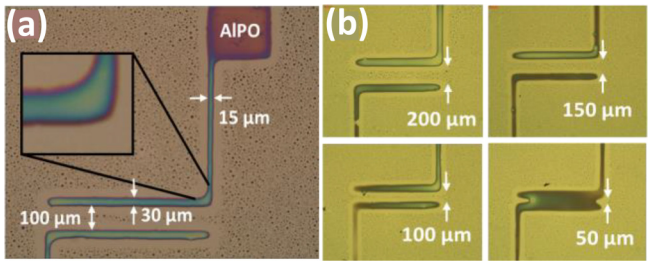

FIG. 8. AlPO thin films deposited selectively as (a) square, line, and 90° bend, and (b) parallel lines of various spacing.

C. Defects

1. Defect density

In the SAM coated hydrophobic regions II, III, and IV (surrounding the AlPO dots and exclusion region as seen in Figs. 3 and 4) are numerous AlPO defect islands. Defects were found to be predominantly circular in shape and ranged in radius, r_{defect}, from less than 0.1 up to ~6 μm, roughly the same order of magnitude as the calculated precursor mist droplet size (less than ~5 μm radius).[19]

Histograms in Fig. 9(a) illustrate the binned size distribution evolution of defect density (number/cm^2), D, in region IV as a function of t_{exp} (for $t_w = 120$ s and [N] = 0.4M). Although the total integrated areal defect density per mm^2, D_{tot}, increases with increasing t_{exp}, the peak of the size distribution remains at $r_{defect} = 2.2$ μm. There appears to be a relative increase in the number of smaller defects of radius less than about 1 μm, as compared to larger defects, consistent with the evolving size distribution of precursor droplets as the fog dissipates over time. It was previously shown that larger droplets settle out of the fog more rapidly than small droplets so that the average droplet size decreases as a function of time.[18] The observation that there is no creation of larger defects with increasing t_{exp} indicates that defect agglomeration is not occurring and suggests that defects are pinned in place and also that the droplets falling on the hydrophobic field region of the substrate are relatively immobile, likely due to the lack of a surface energy gradient to drive motion.

In Fig. 9(b), D_{tot} is plotted as a function of t_{exp}. D_{tot} increases and eventually saturates at long t_{exp}, mirroring film deposition and indicating that defects are continually formed throughout the deposition. D_{tot} decreases rapidly as t_{exp} is reduced, suggesting that thinner films accompanied by lower defect density may be deposited by using a short t_{exp}. The evolution of D_{tot} as a function of t_{exp} in Fig. 9(b) is well fit by

$$D_{tot} = D_{sat}([\mathrm{N}],\ t_w = 120\,\mathrm{s}) \cdot (1 - e^{-t_{exp}/\tau}), \tag{4}$$

where D_{sat} is the defect density at saturation and τ is the characteristic fog settling time (here, 100 s). This equation is analogous to Eq. (1) used previously to model ajFOG film thickness as a function of t_{exp}.[18]

In Fig. 9(c), D_{sat} (for $t_{exp} = 600$ s) is plotted as a function t_w. D_{sat} decreases with increasing t_w and is well fit by

$$D_{sat}([\mathrm{N}],\ t_w) = D_{sat}([\mathrm{N}],\ 0) \cdot e^{-t_w/\tau}. \tag{5}$$

The close fits in Figs. 9(b) and 9(c) of Eqs. (4) and (5) indicate that both defect density as well as film thickness saturate as the fog settles out of the chamber.

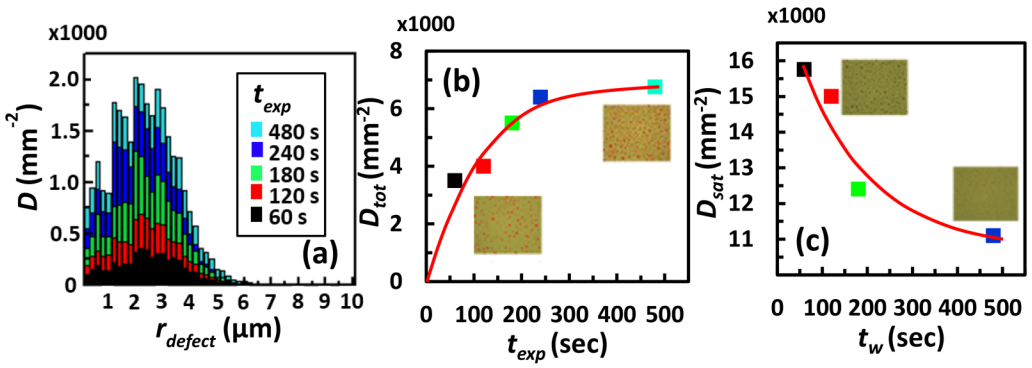

FIG. 9. (Color online) AS-ajFOG deposition of AlPO. (a) Histogram of defect density in the hydrophobic field region as a function of defect radius for t_{exp} ranging from 60 to 480 s. (b) Total defect density as a function of t_{exp}, red solid line shows calculated fit to Eq. (4). (c) Saturated total defect density as a function of t_w, red solid line shows fit to Eq. (5). Insets show processed optical images.

2. Defect origin

An attempt was made to remove the AlPO defects using a post-deposition UV/O_3 exposure to remove the SAM layer (with the assumption that the defects were located on top of the SAM layer). The UV/O_3 treatment did not have any effect on the defects, indicating that the defects are attached to the underlying substrate, rather than the SAM layer. The association of the unwanted AlPO defects with the substrate suggests that their origin may be related to penetration of the AlPO precursor droplets through defects or "pinholes" in the SAM layer.

To assess the influence of the initial SAM quality layer on AlPO island defect formation, defect density was investigated with respect to SAM carbon chain length, application method, and exposure time. The carbon chain length is well known to influence the properties of the SAM coating.[12,14] For example, Jiang and Bent showed that octadecyl-trichlorosilane (OTS-18) was sufficient for AS-ALD of HfO_2, whereas OTS-8 was not.[14] They also showed that increased immersion time in the SAM can improve the quality of a SAM coating and lead to reduced defect density following AS-ALD.[14] For the bulk of the work presented here, OTS-8 SAM was used. OTS-18, which has the same head ($SiCl_3$) and tail (CH_3) groups as OTS-8, but with a longer carbon chain, was also investigated. After confirming that OTS-18 successfully blocked ALD Al_2O_3 while OTS-8 did not, OTS-8 and OTS-18 SAM coatings were then compared for AS-ajFOG deposition using two different application methods: (i) spin-coating at 3000 rpm for 30 s followed by a toluene wash and (ii) immersion for 8, 12, 24, 48, and 72 h [see Fig. S2(a)]. No significant difference in the AlPO defect density or defect size distribution was observed with respect to chain length, application method (spin-coating versus immersion), or immersion time. Note, however, that the contact angle achieved with all of these SAM application methods was typically about 101°. Although 101° represents a highly hydrophobic surface, previous work has shown that contact angles as high as 103.4° and 108.9° are achievable with OTS-8 and OTS-18, respectively.[36] Lower contact angles are an indication of defects in the SAM layer. High pre-ajFOG deposition defect density in the SAM may, therefore, be responsible for the lack of observed differences in D_{tot}. It should be possible to coat SAM layers with higher contact angles (and associated reduced defect densities), which might result in reduced AlPO island defect density in the field following ajFOG deposition. For example, it was reported that while the presence of a trace amount of moisture on the oxidized silicon surface aided in SAM formation, excess moisture in the surrounding atmosphere might promote the formation of 3D aggregates of OTS SAM layers, possibly creating pinholes that thereby affect the overall SAM quality.[37] Conducting SAM formation in a moisture-free environment should thus improve SAM quality and may lead to reduced defect density. In addition, improved surface preparation might be expected to, in turn, improve SAM formation. However, no significant change in defect density or size distribution was observed for a native oxide versus various thicknesses of plasma enhanced atomic layer deposition deposited SiO_2 as the surface layer.

To look at the possibility of unintended damage to the SAM layer surrounding the circular mask openings during the UV/O_3 patterning step impacting the widths and/or average defect sizes of regions II and III, identical depositions were performed on identically prepared SAM layers following 0, 5, 10, and 15 min of patterned UV/O_3 exposure through the mask [see Fig. S2(b)]. AlPO defect island density was found to be independent of UV/O_3 exposure time, indicating that the UV/O_3 exposure does not degrade the SAM layer adjacent to the mask openings.

Finally, no significant change in defect density or size distribution was observed for substrates either held at different angles (0°–60°) or rotated (0–5 rpm) inside the deposition chamber to assist precursor droplets in rolling out of the hydrophobic area, providing further evidence that droplets deposited on the hydrophobic field regions are not mobile.

To summarize, it is found that the AlPO defects islands are (i) not nucleated on top of the SAM layer, (ii) not impacted by the preparation method of the SAM layer, and (iii) not associated with the degradation of the SAM layer prior to deposition due to unintended or incidental UV/O_3 exposure ozone. Because the AlPO defect islands are formed on the substrate underlying the SAM

layer, it is concluded that the origin of the AlPO defects is associated with defects in the SAM, likely those initially present after coating. During deposition, it is likely that precursor droplets penetrate the SAM at defect sites to nucleate AlPO defects on underlying SiO_2. Note, however, that damage to SAM layers has been reported due to harsh process conditions such as during ALD.[14] Thus, it is possible that damage is also occurring during extended ajFOG depositions.

Although the AlPO defect islands do not form a continuous layer and, therefore, may not present a barrier to patterning and integration of low resolution features, even if conductive, there are a number of approaches and strategies that could lead to the reduction or removal of these defects. Improvements in surface preparation and SAM application methods, such as spin-coating in an inert atmosphere with little to no moisture, may lead to improved hydrophobicity and reduced pre-ajFOG deposition defect density in the SAM. The use of SAMs with fluorine terminated tail groups, such as fluoroalkyl silanes, have been demonstrated to show contact angles greater than those achievable for $-CH_3$ terminated SAMs and may also lead to further reduction in defect density.[38,39] Furthermore, new precursor formulations with different concentrations, viscosities, surface tensions, or solvents could lead to smaller defects and reduced defect density.

IV. SUMMARY AND CONCLUSIONS

We have demonstrated area-selective deposition using ajFOG, a solution-based and potentially zero-waste technique in which films are condensed from a uniform aqueous precursor fog at room temperature and near ambient pressure. Selective deposition of AlPO thin films on SiO_2/Si wafers was achieved using a silane-based SAM growth inhibitor patterned by UV/O_3 exposure through a shadow mask. Preferential wetting and nucleation in the hydrophilic regions resulted in deposited features in desired locations with sharp boundaries. Circular dots of AlPO with as small as a 16 μm radius and other shapes such as parallel lines down to a width of 15 μm with separation down to 100 μm, corners, and squares were deposited. Patterned dots were smaller than mask openings and dome shaped with center heights much thicker than expected for the thickness of a blanket deposited film. An unbalanced Young's force due to a surface energy gradient between the adjacent hydrophobic and hydrophilic regions assists transport of material into the patterned feature so that the circular dots have higher volumes than expected for a disk with the radius of the dot. In addition, four regions were observed around each selectively deposited feature. Immediately adjacent to each feature is an exclusion region with no deposition, the width of which is dependent upon the mask and feature size. Beyond the exclusion region, in the surrounding hydrophobic region, are three regions of unintended AlPO defect islands. The size of the defect islands corresponds roughly to the precursor droplet size. The origin of the defects appears to be pre-existing defects in the hydrophobic SAM layer that allow the AlPO precursor to nucleate on the underlying SiO_2. Although the AlPO island defects do not form a continuous layer and may not present a barrier to patterning and integration, even of conductive films, future work will focus on the reduction or removal of these defects. Additional work will also be required to determine the minimum feature sizes and minimum pitches that may be patterned.

In conclusion, we have demonstrated that AS-ajFOG is a promising technique for area-selective, solution-based deposition of micrometer-sized features of various shapes with potential applications for MEMS, flip-chip packaging, and large-area electronics such as displays. In the continuous deposition mode, AS-ajFOG should be compatible with reel-to-reel processing on flexible substrates for large-area electronics.

ACKNOWLEDGMENTS

This material is based on work supported by the U.S. National Science Foundation under Grant No. CHE-1102637. The work was done in the Center for Sustainable Materials Chemistry (CSMC), an NSF Phase-II Center for Chemical Innovation. The authors thank Yu Huang for synthesizing some of the aqueous precursors used in this work.

DATA AVAILABILITY

The data that support the findings of this study are available within the article and its supplementary material.

REFERENCES

[1]A. J. M. Mackus, A. A. Bol, and W. M. M. Kessels, Nanoscale **6**, 10941 (2014).
[2]G. N. Parsons and R. D. Clark, Chem. Mater. **32**, 4920 (2020).
[3]A. Tixier-Mita, S. Ihida, B.-D. Ségard, G. A. Cathcart, T. Takahashi, H. Fujita, and H. Toshiyoshi, Jpn. J. Appl. Phys. **55**, 04EA08 (2016).
[4]F. Liu, C. Nair, H. Ito, B. H. DeProspo, S. Ravichandran, H. Akimaru, K. Hasegawa, and R. R. Tummala, IEEE Trans. Compon. Packag. Manuf. Technol. **9**, 1426 (2019).
[5]W.-H. Kim *et al.*, ACS Nano **10**, 4451 (2016).
[6]A. Mameli, Y. Kuang, M. Aghaee, C. K. Ande, B. Karasulu, M. Creatore, A. J. M. Mackus, W. M. M. Kessels, and F. Roozeboom, Chem. Mater. **29**, 921 (2017).
[7]A. Haider, P. Deminskyi, T. M. Khan, H. Eren, and N. Biyikli, J. Phys. Chem. C **120**, 26393 (2016).
[8]A. Mameli, M. J. M. Merkx, B. Karasulu, F. Roozeboom, W. Erwin, M. M. Kessels, and A. J. M. Mackus, ACS Nano **11**, 9303 (2017).
[9]A. Sinha, D. W. Hess, and C. L. Henderson, Electrochem. Solid State Lett. **9**, G330 (2006).
[10]J. Kwon, M. Saly, M. D. Halls, R. K. Kanjolia, and Y. J. Chabal, Chem. Mater. **24**, 1025 (2012).
[11]C. Cummins, T. Weingärtner, and M. A. Morris, J. Phys. Chem. C **122**, 14698 (2018).
[12]R. Chen, H. Kim, P. C. McIntyre, D. W. Porter, and S. F. Bent, Appl. Phys. Lett. **86**, 191910 (2005).
[13]R. Chen and S. F. Bent, Adv. Mater. **18**, 1086 (2006).
[14]X. Jiang and S. F. Bent, J. Phys. Chem. C **113**, 17613 (2009).
[15]C. Prasittichai, K. L. Pickrahn, F. S. Minaye Hashemi, D. S. Bergsman, and S. F. Bent, ACS Appl. Mater. Interfaces **6**, 17831 (2014).
[16]D. Bobb-Semple, K. L. Nardi, N. Draeger, D. M. Hausmann, and S. F. Bent, Chem. Mater. **31**, 1635 (2019).
[17]I. Zyulkov, V. Madhiwala, E. Voronina, M. Snelgrove, J. Bogan, R. O'Connor, S. De Gendt, and S. Armini, ACS Appl. Mater. Interfaces **12**, 4678 (2020).
[18]N. M. Murari, R. H. Mansergh, Y. Huang, M. G. Kast, D. A. Keszler, and J. F. Conley, Jr., J. Mater. Res. **31**, 3303 (2016).
[19]J. Harra *et al.*, J. Coat. Technol. Res. **15**, 623 (2018).

[20]S. W. Smith, W. Wang, D. A. Keszler, and J. F. Conley, J. Vac. Sci. Technol. **32**, 041501 (2014).
[21]S. Mondal and V. Venkataraman, Appl. Phys. Lett. **111**, 041602 (2017).
[22]N. Hornsveld, W. M. M. Kessels, and M. Creatore, J. Phys. Chem. C **124**, 5495 (2020).
[23]S. T. Meyers, J. T. Anderson, D. Hong, C. M. Hung, J. F. Wager, and D. A. Keszler, Chem. Mater. **19**, 4023 (2007).
[24]K. M. Kim *et al.*, Appl. Phys. Lett. **99**, 242109 (2011).
[25]J. Cho, Y.-W. Kim, B. Kim, J.-G. Lee, and B. Park, Angew. Chem., Int. Ed. **42**, 1618 (2003).
[26]A. T. Appapillai, A. N. Mansour, J. Cho, and Y. Shao-Horn, Chem. Mater. **19**, 5748 (2007).
[27]D. N. Weiss, S. T. Meyers, and D. A. Keszler, J. Vac. Sci. Technol. B **28**, 823 (2010).
[28]S. Mondal and V. Venkataraman, Appl. Phys. Lett. **114**, 173502 (2019).
[29]F. Yaripour, M. Mollavali, Sh. M. Jam, and H. Atashi, Energy Fuels **23**, 1896 (2009).
[30]See supplementary material at https://doi.org/10.1116/6.0000642 for a comparison of FTIR, EDS spectra, and thickness uniformity for AlPO films deposited using fresh and recycled precursors.
[31]C. A. Schneider, W. S. Rasband, and K. W. Eliceiri, Nat. Methods **9**, 671 (2012).
[32]F. Brochard, Langmuir **5**, 432 (1989).
[33]M. K. Chaudhury and G. M. Whitesides, Science **256**, 1539 (1992).
[34]Y. Ito, M. Heydari, A. Hashimoto, T. Konno, A. Hirasawa, S. Hori, K. Kurita, and A. Nakajima, Langmuir **23**, 1845 (2007).
[35]S.-W. Lee and P. E. Laibinis, J. Am. Chem. Soc. **122**, 5395 (2000).
[36]R. Chen, H. Kim, P. C. McIntyre, and S. F. Bent, Chem. Mater. **17**, 536 (2005).
[37]J. Dong, A. Wang, K. Y. S. Ng, and G. Mao, Thin Solid Films **515**, 2116 (2006).
[38]S.-J. Chun, S.-Y. Lee, G.-Y. Jeong, and J. H. Kim, J. Ind. Eng. Chem. **18**, 1122 (2012).
[39]B. D. Booth, S. G. Vilt, J. B. Lewis, J. L. Rivera, E. A. Buehler, C. McCabe, and G. K. Jennings, Langmuir **27**, 5909 (2011).